TECHNOLOGY DEVELOPMENT FOR EXOPLANET MISSONS

Optical Vortex Phase Mask Development and Testing

Gene Serabyn[1]
Dimitri Mawet[1,2]
Garreth Ruane[1]
Jorge Llop-Sayson[1]
Kent Wallace[1]
Lorenzo Koenig[1]
Niyati Desai[1]

[1]*Jet Propulsion Laboratory, California Institute of Technology*
[2]*California Institute of Technology*

June 25, 2025

National Aeronautics and Space Administration
Jet Propulsion Laboratory
California Institute of Technology
Pasadena, California

Jet Propulsion Laboratory
California Institute of Technology

Approvals:

Released by

E-SIGNED by Eugene Serabyn
on 2025-07-10 08:55:47 GMT

Gene Serabyn **Date**
Principal Investigator

Approved by

E-SIGNED by Brendan Crill
on 2025-07-09 13:41:00 GMT

Brendan Crill **Date**
Exoplanet Exploration Deputy Program Chief Technologist, JPL

E-SIGNED by Nicholas Siegler
on 2025-07-09 14:56:19 GMT

Nick Siegler **Date**
Exoplanet Exploration Program Chief Technologist, JPL

E-SIGNED by Lucas Paganini
on 2025-07-09 16:24:46 GMT

Lucas Paganini **Date**
Exoplanet Exploration Program Executive, NASA HQ

Table of Contents

TDEM Milestone White Paper:
Optical Vortex Phase Mask Development and Testing

1. Objective

In support of NASA's Exoplanet Exploration Program and the ROSES Technology Development for Exoplanet Missions (TDEM) program, this whitepaper explains the purpose of the planned TDEM Milestones for the project entitled ***Optical Vortex Phase Mask Development and Testing***, specifies the methodology for computing the milestone metrics, and establishes the success criteria against which the milestones will be evaluated. For consistency, the methodology for computing the milestone metrics used here is identical to the methodology of our previous 2019 vortex coronagraph TDEM whitepaper, ***Vortex Coronagraph High Contrast Demonstrations***.

The top priority of the 2020 Decadal Survey for Astronomy & Astrophysics (ASTRO2020)[1] is the imaging and spectroscopy of terrestrial exoplanets in the habitable zones of nearby stars. The milestones described herein are therefore aimed at demonstrating improved optical vortex coronagraph performance (i.e., deeper contrast and broader bandwidth) for potential use in future exoplanet space missions such as the Habitable Worlds Observatory[2] (HWO). However, spectroscopic measurements of terrestrial exoplanets ~ 10^{-10} as bright as their host stars are so challenging that the needed broadband contrasts have yet to be demonstrated in the laboratory[3]. Achieving the requisite starlight suppression level in the laboratory is thus essential to demonstrating the viability of future exoplanet missions. This work is therefore aimed at the Strategic Astrophysics Technology Tier 1 Technology Gap of "Coronagraph Contrast and Efficiency", aiming at both improved contrast and higher efficiency.

As the critical component in any vortex coronagraph is the optical vortex phase mask, our basic goal here is to develop and test improved vortex phase masks. However, as HWO's eventual observational goals[2] might potentially cover about three octaves of wavelength, from ~ 0.2 μm in the near-ultraviolet to ~ 1.8 μm in the near-infrared (NIR), different mask fabrication technologies may need to be called upon to cover this range. Our work therefore has two main thrusts. The first is to develop improved vortex masks using three different promising fabrication technologies, to identify the best route or routes to vortex mask fabrication. The second is to show that a vortex phase mask of at least one of these types can reach or get close to the performance called for by observations of terrestrial exoplanets, which is a contrast of ~ 10^{-10} for 20% bandwidth (BW).

Of course, realistic performance milestones cannot exceed the best performance that the testbed used is capable of, and so our milestone levels are chosen to be consistent with the best recent contrast performance[4] of JPL's Decadal Survey Testbed (DST), i.e., a few × 10^{-10}. Such levels are also consistent with a recent DST error budget estimate[4] (see Table 1), and approach the intrinsic planet/star contrast ratios expected for terrestrial exoplanets around sun-like stars. We therefore aim at rejection demonstrations to "testbed best" levels, first for 10% BW light, and then for 20% BW. Of course, should the intrinsic testbed performance improve in the future, our vortex coronagraph performance targets can follow suit, aiming at an ultimate ~ 10^{-10} contrast.

	Error source	Contrast contribution
Testbed hardware	DM electronics	$\sim 1 \times 10^{-10}$
	Other incoherent background	$\sim 1 \times 10^{-10}$
Coronagraph design	FPM substrate ghost	$\sim 1 \times 10^{-10}$
	Coronagraph chromaticity	$\sim 1 \times 10^{-10}$
	Total:	4×10^{-10}

Table 1. *Current DST error budget estimate (from ref. 4).*

2. Milestone Definitions

TDEM Technology Milestones are intended to document progress in the development of key technologies for a space-based mission such as HWO that would spectroscopically characterize terrestrial exoplanets, thereby gauging the mission concept's readiness to proceed from pre-Phase A to Phase A. This TDEM's milestones address starlight suppression with the optical vortex coronagraph, its ultimate objective being the validation of the focal-plane vortex phase mask with broadband light for a clear, monolithic, off-axis aperture. Our milestones therefore focus on the validation of the key TDEM technology component - the vortex phase mask, and our three milestones aim at high contrast and increasing bandwidth. Success is defined in terms of quantified performance demonstrations employing this key component. These demonstrations will need to be carried out in state-of-the-art high-contrast testbeds that are maximally isolated from extraneous environmental factors such as vibration, pointing and temperature fluctuations.

Our specific milestones are tied to our current best demonstrated broadband performance with a vortex mask in the testbed (1.6×10^{-9} contrast for 10% BW; Sect. 3.3) and to the best current contrast performance of JPL's DST (Table 1), which implies best achievable monochromatic and broadband testbed contrasts of 2×10^{-10} and 4×10^{-10}, respectively. Note that the testbed's best performance is partially limited by the vertical resolution of the testbed's deformable mirror (DM). Allowing for a margin of 1×10^{-10}, a realistic broadband contrast milestone level is thus 5×10^{-10}. To improve performance, we must proceed in two directions, i.e., improved contrast and improved BW, so our plan is to start with a pair of intermediate milestones that each improve performance along one of these axes, and then to push to deep broadband contrast as our final milestone. As such, to validate vortex mask performance, we therefore plan the following three milestones:

Milestone 1: Suppression of 20% bandwidth light with a Vortex Phase Mask

Using an optical vortex phase mask, and a point source illuminating a clear monolithic input pupil, demonstrate a calibrated average coronagraph contrast of 1.6 × 10^{-9} over separations of 3 – 10 λ/D, for 20% bandwidth light of at least one polarization state anywhere in the wavelength range 300 –1000 nm.

Milestone 2: Deep suppression of 10% bandwidth light with a Vortex Phase Mask

Using an optical vortex phase mask, and a point source illuminating a clear monolithic input pupil, demonstrate a calibrated average coronagraph contrast of 5× 10^{-10} (i.e., as deep as the DST currently allows) over separations of 3 – 10 λ/D, for 10% bandwidth light of at least one polarization state anywhere in the wavelength range 300 –1000 nm.

Milestone 3: Deep suppression of 20% bandwidth light with a Vortex Phase Mask

Using an optical vortex phase mask, and a point source illuminating a clear monolithic input pupil, demonstrate a calibrated average coronagraph contrast of 5× 10^{-10} (i.e., as deep as the DST currently allows) over separations of 3 – 10 λ/D, for 20% bandwidth light of at least one polarization state anywhere in the wavelength range 300 –1000 nm.

The angular extent of the dark hole, illustrated in Fig. 1, is defined in terms of the wavelength λ and the diameter D of the aperture stop on the DM, which defines the pupil in the laboratory coronagraph. Our performance metric is the average contrast in the dark hole specified in these milestones. Contrast is defined for any point in the field as the calibrated ratio of the residual light level at that location to the light level at the peak pixel of the point-source point spread function in the absence of a coronagraphic mask (Sect. 5).

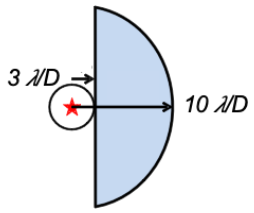

Figure 1. *Target high-contrast dark field from 3 to 10 λ/D. The location of the suppressed central star is indicated in red.*

2.1. Relevance for a Future Exoplanet Mission

Development of vortex technology is intended to advance the readiness of mission concepts for the coronagraphic imaging and spectroscopy of exoplanetary systems. The small inner working angle (IWA) capability of the vortex coronagraph allows consideration of a range of mission sizes, from probe-scale (Exo-C[5]) to flagship-scale missions (Habex[6],

LUVOIR[7] and HWO). Exact terrestrial exoplanet analogs with an albedo of 0.3 occur at a contrast of $\approx 2 \times 10^{-10}$, motivating our milestone demonstration levels, which are as close to this level as is currently possible with the DST.

Exoplanet imaging missions use a DM to form a high contrast "dark hole" or "dark field" over a working angle spanning ~ $n_I\lambda/D$ to $n_O\lambda/2D$, where n_I sets the IWA, as defined by the science requirements, the intrinsic capabilities of the coronagraph, and the wavefront and pointing control capabilities of the mission, and n_O sets the outer working angle (OWA). The OWA is defined by the highest spatial frequency controlled by the DM aperture selected. n_O is typically somewhat smaller than $n_{DM}/2$, where n_{DM} is the number of actuators across the DM, in order to allow for finite gradients in the transition from the dark hole region to the outer much brighter region.

Our previous vortex-milestone dark holes specified IWAs of $3\lambda/D$. Somewhat smaller IWA values are theoretically possible with the vortex coronagraph, but as our main goals here are contrast and bandwidth performance, we use IWA = $3\lambda/D$ here as well. For the OWA, we take the OWA of the previously demonstrated DST dark hole[4], i.e., $10\lambda/D$. Both the 48 × 48 element Xinetics DM and the 50 × 50 element Boston Micromachines DM can reach this OWA, as their theoretical maximum OWAs are $24\lambda/D$ and $25\lambda/D$, respectively.

The OWA also impacts the testbed's collimated beam diameter, and so could impact the diameters of any circular polarizers used. However, in the testbeds (see Section 3), the initial circular polarizer lies in a small-diameter collimated beam prior to the source pinhole, and the second circular polarizer lies in the reduced-diameter beam downstream of the Lyot stop, so standard 1-inch optics should be fine.

3. The Optical Vortex Coronagraph

One of the most promising stellar coronagraphs is the optical vortex coronagraph[3,8-11], which had been selected as the primary or secondary coronagraph by both the Habex and LUVOIR mission concept studies. This section describes its theory of operation and the core component – the optical vortex phase mask.

3.1. Optical Vortex Coronagraph Theory

The operation of an ideal optical vortex coronagraph is described in detail in, e.g., refs. 8-11. A clear telescope input pupil can be described by a field distribution, $P_i(r)$, of

$$P_i(r) = \begin{cases} 1 & \text{for} \quad r < a \\ 0 & \text{for} \quad r > a, \end{cases} \tag{1}$$

where r is the radial coordinate, and a is the radius of the input aperture. Focusing the light leads, via a Fourier transform, to the usual focal-plane field distribution,

$$E_f(\theta) \propto \frac{J_1(ka\theta)}{ka\theta}, \tag{2}$$

where J_1 is the Bessel function of order 1, k is the wavenumber, and θ is the angular radial offset from the center of the stellar PSF.

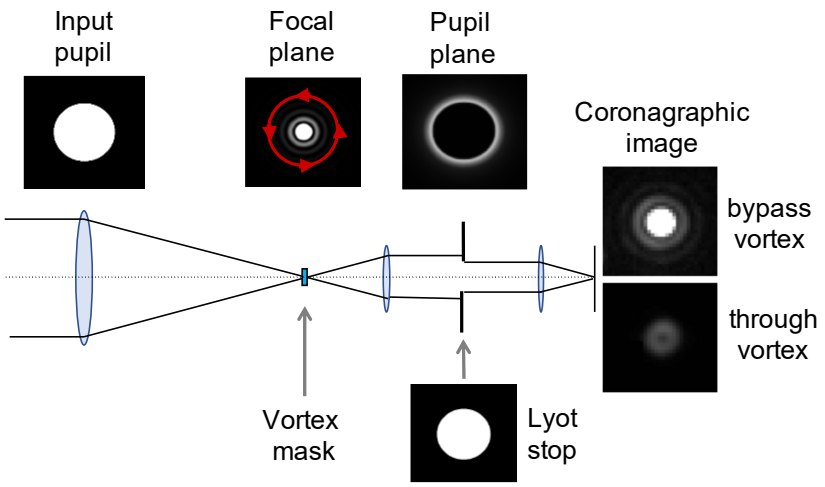

Figure 2. *Layout and operation of the optical vortex coronagraph: an optical vortex phase mask with a 2πn phase wrap (red) around the center of the focal plane image of the star yields a downstream pupil image in which all of the on-axis starlight appears outside of the original pupil's image, where it is blocked by an aperture (Lyot) stop.*

Passing this focal plane field distribution through a centered optical vortex phase mask (Fig. 2) modulates the field with a phase factor corresponding to an azimuthal phase ramp, i.e., nα, where α is the azimuthal angle, and n is the "topological charge" of the vortex (the number of 2π phase wraps that the mask generates in a circuit about the center), yielding

$$E_f(\theta, \alpha) \propto e^{in\alpha} \frac{J_1(ka\theta)}{ka\theta}. \tag{3}$$

After the vortex phase mask, the light is recollimated and forms a downstream pupil image. Because of the Fourier transform relationship between focal and pupil planes, the vortex's phase wrap, and the following property of Bessel functions, J_n, of order n,

$$J_n(x) = \int_{-\pi}^{\pi} e^{-i(n\varphi - x\sin(\varphi))}\, d\varphi, \tag{4}$$

the reimaged pupil plane distribution is proportional to

$$\int_0^{\infty} J_n(kr\theta) J_1(ka\theta) d\theta \tag{5}$$

instead of the usual

$$\int_0^{\infty} J_0(kr\theta) J_1(ka\theta) d\theta. \tag{6}$$

This modest change to the integrand alters the downstream pupil intensity distribution dramatically, in the ideal case (for even n only) moving all of the on-axis starlight from inside the entrance pupil to its exterior (Fig. 2, top right panel.) Outside the post-vortex pupil, the electric field falls off as rippled power laws, leading to multiple azimuthal rings

for n > 2. In the ideal case, the starlight can then be completely blocked in the downstream pupil plane by a simple aperture stop slightly smaller than the pupil image.

However, pointing errors and wavefront aberrations will leave residual light inside the pupil in the real world, which wavefront control will be needed to reduce. Higher charge vortex masks have larger IWAs, and so are also less sensitive to pointing errors and low-order aberrations[12], making charges 4 and 6 of interest for exoplanet space missions.

3.2. Optical vortex masks

Optical vortex phase masks come in two main flavors: the scalar vortex (SV) mask, which introduces the needed spatial phase pattern using longitudinal phase, i.e., pathlength, and the vector vortex (VV) mask, which uses geometric phase. The needed azimuthal phase spiral can be fabricated in several ways[13] (Fig. 3). Of these, the most technically mature type of vortex mask is the VV mask, which we have pursued in our previous TDEM work, and two types of VV mask have been deployed on large ground-based telescopes[14-18], those being masks made with form birefringence (for longer infrared wavelengths where the desired structures are larger)[10,15,16], and spatially-variant liquid-crystal-polymer (LCP) diffractive waveplates (used at shorter, i.e., NIR and visible wavelengths)[11,19]. In contrast, SV masks have seen only limited trials on telescopes[20]. Scalar vortex masks can also be made in a number of ways, e.g., using thickness variations[21,22] in glass or dielectrics, or as spatially-variant metasurfaces[23,24] (Fig. 3). Metasurfaces can be thought of as artificial materials wherein the index of refraction and its lateral spatial variations can both be selected by design.

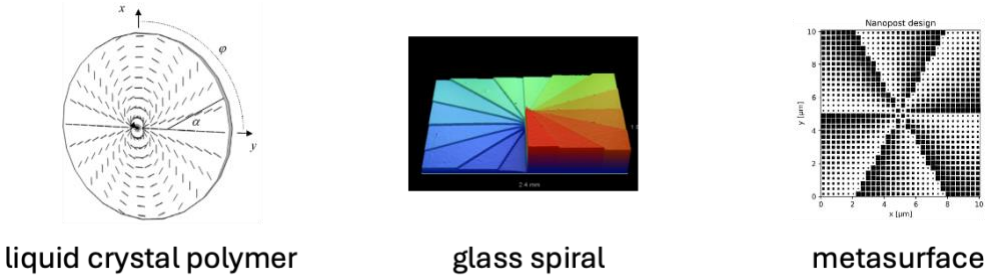

Figure 3. *Different types of vortex mask. Other techniques are also possible.*

3.3. Contrast performance to date

The best laboratory vortex coronagraph contrasts achieved to date (Fig. 4) have also been with VV masks, specifically, a monochromatic contrast[25] of 2.5×10^{-10} and a broadband (10% BW) contrast[26] of 1.6×10^{-9}. The residual leakages seen in the two cases are quite different, with monochromatic rejection limited by a residual Airy-like pattern, due either to polarization leakage or central-defect leakage, while broadband rejection is limited by small, localized off-axis bright spots that cannot be corrected broadband by a DM.

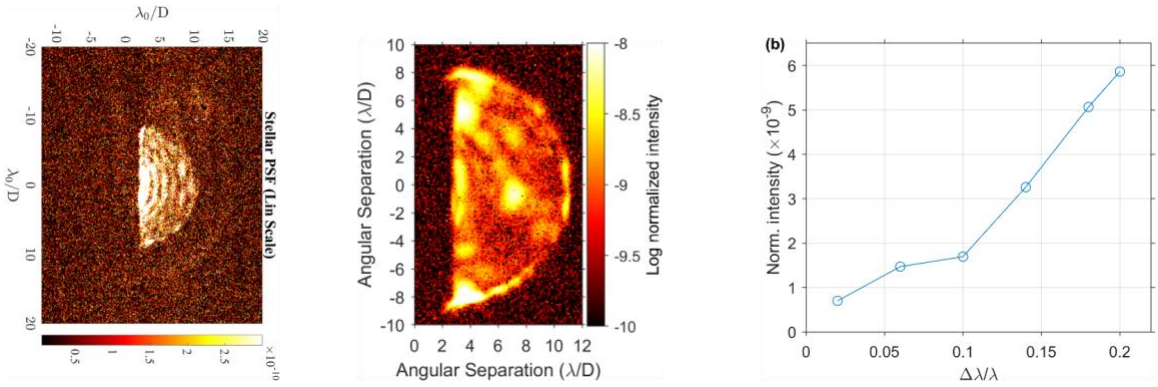

Figure 4. *Current best vortex mask contrast performances showing the dominant leakages. Left: 2.5 x 10^{-10} contrast monochromatic dark hole that is limited by residual Airy rings. Center: 10% BW, 1.6 x 10^{-9} dark hole that is limited by small localized bright spots. Right: Best vortex coronagraph contrast as a function of bandwidth.*

3.4. The Plan

Even better performance is needed for terrestrial exoplanets, specifically, another factor of ten in broadband starlight suppression, and a doubling of the instantaneous suppression bandwidth. Therefore, to make progress, we can no longer limit our choices to just one type of vortex mask. This is doubly important as different technologies may work better at the different wavelengths across the potentially broad HWO passband, and increasing the number of potential vendors would also help to strengthen the commercial supply chain for vortex masks. Therefore, we plan to develop not only our already high-performance VV LCP masks, but also less mature SV masks, following up on our previous APRA work.

But, why pursue SV masks, if they are less mature and highly chromatic? It turns out that because VV masks apply phase ramps of opposite sign to the two circular polarization states, they likely engender the need for polarization splitting. This unfortunately necessitates either a doubling of part of the optical system (thereby raising costs significantly), or the elimination of one of the two polarization states (which decreases sensitivity). This makes polarization-independent vortex masks highly desirable, which makes developing polarization-independent SV masks a high priority. But, one trades a polarization problem for a chromaticity problem, for which a viable solution is needed.

After wide-ranging investigations, we have recently developed two theoretically-promising, i.e., less chromatic, SV solutions[24,27]. The first is based on a pair of thin glass (or dielectric) azimuthal-sawtooth phase masks that include a central π-radian phase step[27] (i.e., a central "dimple"), and the second is the use of artificial dielectric materials made of metasurface nanoposts[24]. In addition to continuing to pursue higher performance VV masks, we will therefore also pursue the development of these two SV technologies. However, as the best mask technology may be a function of wavelength (and time), our primary goal in this project is to show that at least one of these three fabrication methods

is able to produce a vortex mask that can reach "DST best" contrast levels. We now describe each of these three mask types and the work planned.

3.5. The Two-Glass Scalar Vortex Mask

Achromatic solutions for SV masks exist in theory, which are based on using pairs of glasses[28]. However, the classical solution requires the glasses to have azimuthal spiral structures that have heights that are excessively large (~ mm), i.e., much too large to be manufacturable by typical etching techniques. Our goal is then to find a physical mask structure that can provide deep rejection over a broad band, while also being feasible to fabricate. A critical insight comes from calculating SV masks' azimuthal Fourier power spectrum[27], which led us to suggest combining the azimuthal phase spiral of an SV mask with the radial phase structure of a central Roddier[29] π-phase "dimple", as in Figs. 5 and 6, in order to suppress the zeroth-order azimuthal term. (This term yields leakage in off-center wavelengths.) The radius of the needed phase dimple roughly divides the power in the stellar point-spread function in half[27,29]. As Table 2 and Fig. 6 show, such modified masks are predicted to improve contrast over a plain vortex sawtooth mask by a factor of ~ 100.

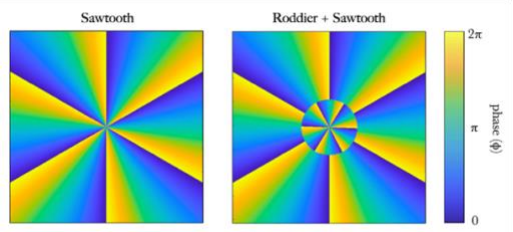

Figure 5 *Phase maps of scalar vortex masks consisting of a) a sawtooth azimuthal vortex pattern (which is structurally analogous to an azimuthal Fresnel lens) and b) the same sawtooth vortex with a central phase dimple added.*

Average raw contrast 3-10 λ/D

	10%	20%
Vortex	4.06e-7	1.17e-6
Sawtooth	2.03e-7	1.00e-6
Roddier + Sawtooth	3.77e-9	3.79e-8

Table 2 *Average contrast predicted[27] in the 3-10 λ/D region for a classical single-ramp vortex, a sawtooth vortex (Fig. 5, left side), and a sawtooth vortex with a central Roddier dimple (Fig. 5, right side and Fig. 6, left side), for 10% and 20% BW.*

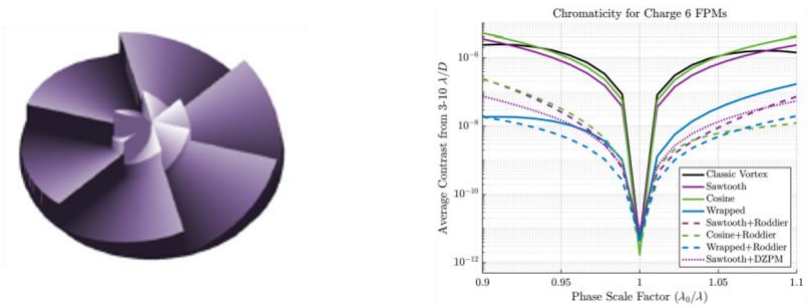

Figure 6 *Left: Dimpled sawtooth vortex surface profile. Right: Predicted contrast over 3 – 10 λ/D as a function of wavelength over a 20% BW.*

An initial mask of this type has been fabricated for us by Zeiss GmBH, and we have tested it in JPL's In Air Coronagraphic Testbed (IACT), reaching a contrast[27] of 2 x 10^{-7} with a 10% BW. However, in the course of this work, we found a design flaw, and are now awaiting a second generation of mask that should allow us to reach the predictions of Table 2. While allowing us to test the model, the predicted performance of single-glass dimpled-sawtooth SV masks is still short of that needed for terrestrial exoplanet observations. To reach even deeper rejection over a broad passband, we will need to use pairs of such masks made of different materials of high refractive index (to allow lower thicknesses) and high Abbe numbers (for low dispersion). The Abbe number, V_d, defined as

$$V_d = \frac{n_d - 1}{n_F - n_C},$$

where n_C, n_d, and n_F are the refractive indices at the wavelengths of the Fraunhofer C, d, and F spectral lines (656.3 nm, 587.56 nm, and 486.1 nm respectively), is an approximation to reciprocal of the slope of the refractive index vs. wavelength across the optical regime, and so provides a measure of the material dispersion.

Searches through optical material catalogs have yielded three material pairs that can reach contrasts < 10^{-10} across a 10% passband (Fig. 7) with dimpled-sawtooth SV structures of reasonable profile heights, i.e., a few microns each instead of millimeters. With a profile height reduction of 2 orders of magnitude, such masks should be manufacturable, and both vortex surfaces can lie within the stellar depth of focus, as also needed. Fig. 7 illustrates this two-material structure, with the two colors showing the two different material surfaces.

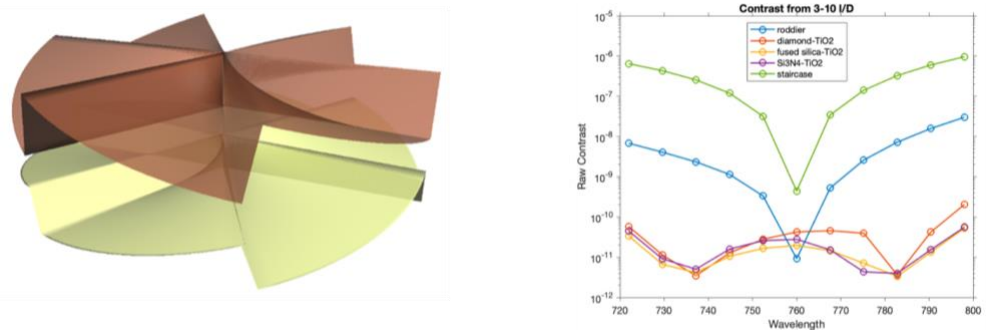

Figure 7 *Left: Vortex surfaces of a pair of sawtooth SV masks (the two different dielectric surfaces are shown in two different colors; to avoid clutter, the central dimples are not shown). Right: Predicted contrast over 3 – 10 λ/D for a 10% BW.*

Based on this theoretical progress, our goal is now to make SV masks out of promising glasses and dielectrics and to test them, first in the IACT, and then in the DST, when they achieve the requisite quality. To do this, first, we will more thoroughly search all glass and dielectric catalogs to look for optimal dual-material solutions, and then we will contact and work with vendors (including JPL's Microdevices Lab (MDL) and Caltech's Kavli Nanoscience Institute (KNI)) to manufacture the designed vortex pair. Besides testing both the model and the fabrication techniques, such masks should eventually lead to demonstration of the needed contrast in the DST.

3.6. The Metasurface Scalar Vortex Mask

Because finding just the right combination of dielectric materials to provide the desired SV azimuthal phase structures with easily manufacturable thicknesses is quite difficult, we are also investigating another approach to making SV masks - metasurfaces, which are thin layers of subwavelength nanoposts designed to apply a specific phase and amplitude pattern to an incident beam (Fig. 3, right hand image, and Fig. 8).

Metasurfaces can provide full 2π phase coverage, with high throughput[30-32]. Several applications of metasurfaces in generating vortex beams have been reported[33-35] and recently significant progress has been made in making metasurface components achromatic across large bandwidths[36-38]. Compared to SV masks using glass phase delays, a metasurface can theoretically have a better achromatic performance within a single layer due to the additional freedom introduced by different nanopost geometries (Fig. 8). As metasurfaces can be engineered to provide 0 to 2π phase coverage with high throughput across large bandwidths, they can address the primary goal of SV masks, making them a candidate for achromatic high-performance coronagraphs, as shown by an early model simulation of performance in Fig. 9. Moreover, as metasurfaces of circular or square nanoposts are polarization-independent, such SV masks could eliminate the need to remove or split polarization states.

Figure 8. *A range of possible nanopost geometries based on round or square symmetry (adapted from ref 37).*

We will first theoretically explore broadband metasurface SV mask designs that can potentially meet HWO requirements. To do this, we will model a range of polarization-independent metasurface geometries (with square/round nanoposts) to calculate their phase responses and transmissions vs. wavelength, using rigorous coupled-wave analysis (RCWA), which is a suitable tool to obtain the phase and transmission of locally periodic subwavelength structures. RCWA will also be used to calculate broadband contrast for the

achromatic helical phase ramp caused by our spatially variant metasurface structure (Fig. 3). The potential improvement of metasurface masks over classical SV masks (without a central dimple) is seen in Fig. 9, which shows a performance improvement of up to two orders of magnitude across a 20% BW for the case of square nanoposts. More complex geometries provide further degrees of freedom that will also be explored.

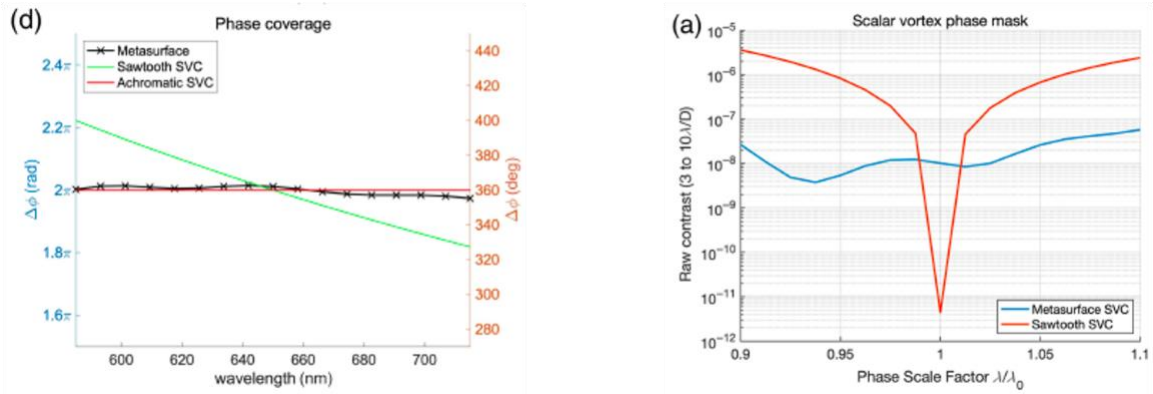

Figure 9. *Left: comparison of phase performance of a classical sawtooth SV, a (non-realistic) theoretically achromatic SV mask, and a metasurface SV mask. Right: Blue curve: Simulated contrast of a charge 6 SV phase mask based on square nanoposts over 20% BW. Red curve: comparable result for classical sawtooth vortex.*

These calculations will be augmented with the finite-difference time-domain (FDTD) method to calculate the effect of the discontinuities in the vortex pattern. Though computationally expensive, FDTD provides valuable insight into the interaction of the metasurface blocks with their environment, particularly important in the region of the phase pattern discontinuity. Finally, we will propagate the fields obtained from these simulations with the Fast Linearized Coronagraph Optimizer[40] package to assess the mask's coronagraphic performance under realistic conditions. The described simulation framework is a crucial tool to identify suitable SV metasurface designs. These tools have previously been used to optimize VV masks based on form birefringence[15,16], and we will now apply them to the design of metasurface SV coronagraphic masks.

Being able to actually fabricate the designed SV masks is of course also crucial. Candidate materials include Si, TiO_2 and diamond, each with its own advantages and disadvantages, related to wavelength of operation and achievable post and gap sizes. Indeed, the most promising material and manufacturing approaches depend on the specific target waveband within HWO's potential 0.2-1.8 micron range, so different materials will likely be necessary. As long wavelengths allow for larger and more easily manufacturable structures, we will start with a NIR metasurface prototype made out of TiO_2 or Si, using the microfabrication facilities at MDL and KNI. We will then characterize the resultant phase response using metrology to understand the limitations and uncertainties of both the simulations and the manufacturing process before moving on to shorter wavelengths. To obtain a high-performance component, several iterations adapting the design process to the manufacturing constraints will be needed, and so we expect the development of this type of mask to take longer than that of the other types.

3.7. The Vector Vortex LCP Mask

Our previous TDEM work focused mainly on VV masks made of birefringent LCP layers (Fig. 10). Our LCP vector vortex masks are fabricated by orienting the optical axis pattern using UV alignment, with the topological charge selected by virtue of the azimuthal rotation rate of the LCP monomers. The pattern is then locked in place by polymerization, resulting in a solid LCP layer. An actual charge 6 LCP vortex mask manufactured by Beam Engineering (Beamco) is seen between crossed polarizers on the right-hand side of Fig. 10.

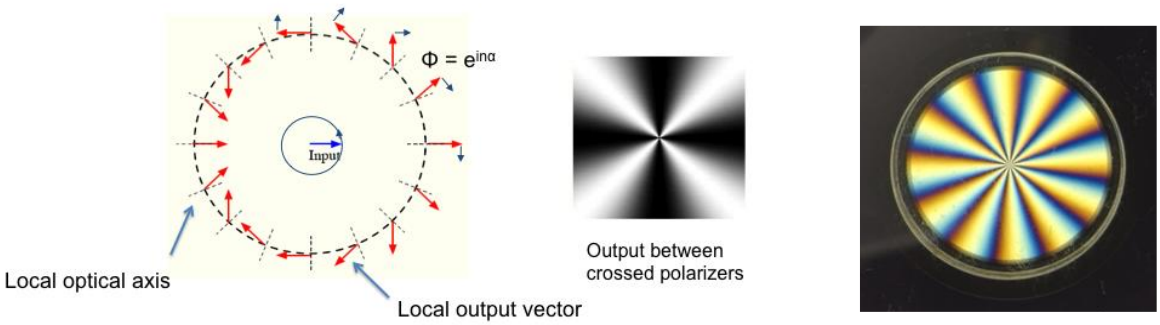

Figure 10. *Left: Operation of a charge 2 vector vortex phase mask. The output field (red arrows) rotates twice as fast as the optical axes (thin radial dashed lines). Center image: model of a charge 2 vortex between crossed polarizers. The output field rotates twice in a circuit about the center, so the output field is parallel to the output polarizer 4 times, yielding 4 radial bright bands. Right: A three-layer charge 6 LCP vector vortex mask manufactured by Beamco, as seen through crossed polarizers. With 6 rotations of the transmitted field in one circuit about the center, 12 transmission maxima are present.*

However, as our LCP masks have not yet reached the ultimate contrast performance, they have limitations that need to be improved, including imperfect geometric patterns, bandwidth limitations, and imperfect layers.

First, as no physical vortex pattern can be geometrically perfect all the way in to the central singularity, a small central defect must be present in the vortex pattern. Beamco has managed to reduce the diameter of this central defect to only a few microns. Common wisdom suggests that this defect should then be masked off with a small central opaque dot mask, as is illustrated in Fig. 11 (top), as the center of the mask is where the starlight is brightest. However, our best recent laboratory contrasts were obtained with a mask lacking a central dot mask, although the performance difference to the next best masks have recently only been on the order of a factor of 2. It would therefore be desirable to establish whether a central blocker is actually needed, as its absence would simplify mask design.

The tight layer tolerances involved in fabricating a 3-layer mask means that a one-to-one comparison is best done on the same mask. To this end, a mask was designed that can be disassembled (Fig. 11, bottom). I.e., the black dot is placed on a separate substrate from the vortex layers (as usual), but rather than gluing them together, an air gap is left, with the two substrates held together by a few tacks of glue along the rim (Fig. 11, right). With this mask, we can thus carry out contrast tests in the DST with a fully assembled mask, and then remove the spots of glue and retest the vortex mask without the central dot layer. So

far, we have carried out some initial tests with the dot in place, but limited testbed time has so far not allowed a complete measurement suite. Once this phase is complete, we will remove the glue tacks, and proceed to the no-dot comparison test.

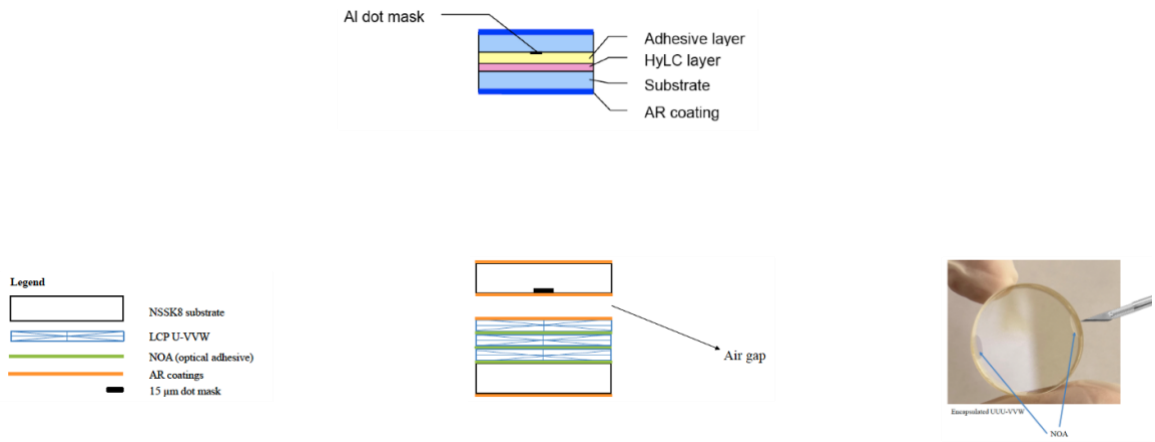

Fig. 11. *Mask cross-sections for our masks to date (top), and for a mask with a removable central opaque spot (bottom). An air gap separates two substrates, which are tacked together at their edges. First the mask will be tested assembled, and then the glue will be removed, and the mask retested without the central opaque spot substrate.*

Second, any half-wave plate (HWP) has bandwidth limitations. To broaden the bandwidth, we have been using the classical three-layer HWP prescription of Pancharatnam[41], in which the optical axes in each layer are rotated with respect to each other by angles of ~ 0°, 60°, and 0°, as is seen in Fig. 12 for the case of uniform HWPs (top), and vortex HWPs (bottom row).

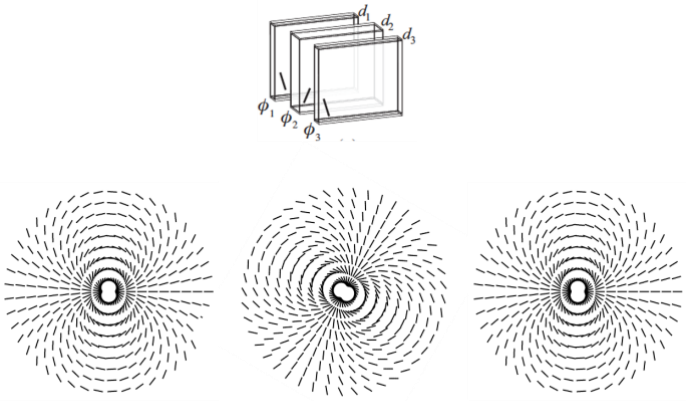

Figure 12. *top: classical uniform multilayer approach to broadening waveplate passbands (from ref 42). The optical axis orientations in the successive layers are shown. Bottom: the optical axes in the three layers of a broadband charge 4 vortex. Note that everywhere in the plane, the optical axes shift by the same amounts between successive layers.*

However, for any wavelength where the individual HWP layers do not provide a perfect π phase shift, some light leakage remains in the original polarization state. (Recall that a perfect HWP reverses circular polarization states.) Fortunately, this leakage (which produces an Airy pattern in the focal plane, as the leakage uniformly fills the pupil) can be reduced using the technique of spectral polarization filtering (Fig. 13) wherein a circular polarizer removes the leaked light still in the pupil. (The bulk of the starlight that "sees" the vortex's π phase shift ends up in the opposite circular polarization state outside the pupil [Fig. 2], where the Lyot stop blocks it.) However, for this to work well, high-quality quarter-wave plates (QWPs) and polarizers are needed to act as circular polarizers. Unfortunately, high quality QWPs are as difficult to acquire as high quality vortex masks, so the total leakage must be budgeted between all of the retarders present.

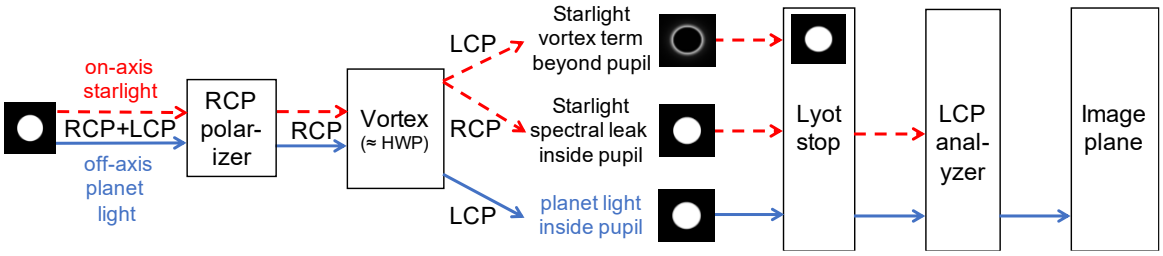

Figure 13. *Spectral polarization filtering. The starlight is shown in red, and the planet light in blue. RCP and LCP stand for right circular polarization and left circular polarization, respectively. The starlight outside the pupil is rejected by a Lyot stop, while the spectral starlight leakage inside the pupil is rejected by a circular polarizer*

Hitting exactly a half wave of retardance, i.e., the correct vortex layer thicknesses, is a challenge mainly because of the high sensitivity of layer parameters to manufacturing tolerances. This can be seen in Fig. 14, where a Monte Carlo simulation for three different levels of parameter errors shows how quickly the desired design degrades[43]. Such fine layer tolerances make it very difficult to hit exact retardance targets, and also to make masks reproducible to a high degree. As a result, the approach so far has been to make a large number of masks, so as to get close to the target with at least one of them. However, as this is time consuming, costly, and not guaranteed, an improved approach is needed.

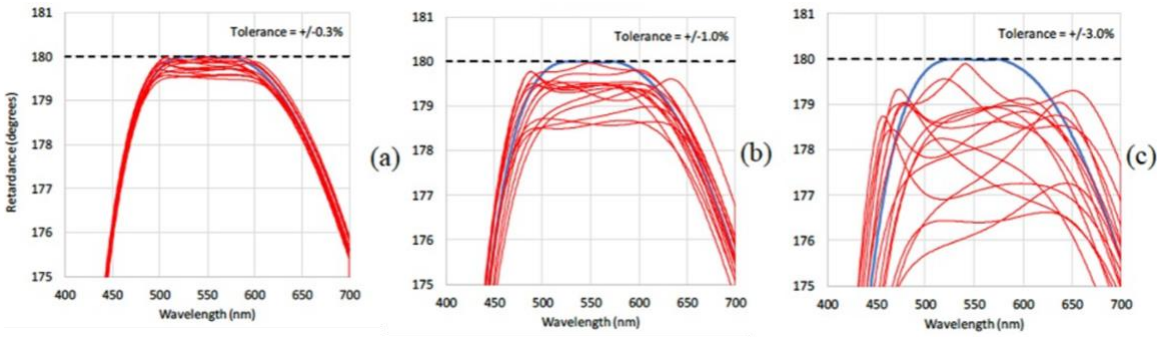

Fig. 14. *Mask retardance vs. wavelength[43] expected for repeated fabrication runs with manufacturing layer tolerances of 0.3% 1.0% and 3.0% (left to right).*

One path to broader bandwidths is to increase the number of HWP layers making up the VV mask to 5. The effect on bandwidth is illustrated in Fig. 15, where a rough doubling of the bandwidth is seen[44], in both the theoretical design and in the measurements of an initial 5-layer mask. This step should thus allow us to achieve our first broader-band milestone. We note that this possibility has not yet been pursued vigorously in practice because more layers make for a yet more complicated fabrication process, with increased risk of contamination. But with improved layer qualities now, this approach should be feasible. However, manufacturing tolerances remain uncomfortably tight.

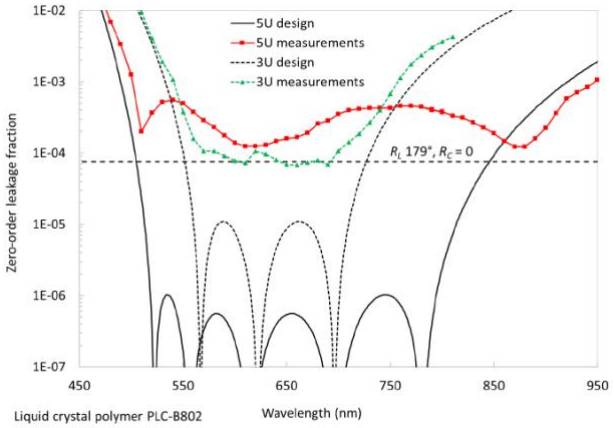

Fig. 15. *Zero-order leakage vs. wavelength for LCP VV masks made of 3 and 5 vertically uniform (U) layers.[44] Both theoretical and experimental results are shown.*

On the other hand, in searching parameter space for a way to relax tolerances, a different very interesting possibility emerged. Specifically, in the three-layer broadband vortex masks fabricated so far, the topological charges of the three layers have always been identical. But what if they are not? It turns out that dropping this constraint opens a large new area of parameter space that leads to a very interesting theoretical conclusion. First, note that any 3-layer HWP mask will have 2^3 total transmitted terms, due to one bright transmission and one leakage term at each of its 3 layers. The 8 terms transmitted by the 3-layer HWP structure will then consist of one desired bright vortex term (that is sent outside the pupil image) and 7 dim leakage terms. As is illustrated in Fig. 16, it turns out that 6 of these leakage terms can be sent outside the pupil if the layers all have differing charges, as three of the seven leakage terms caused by layer inaccuracies change from terms with uniform-phase pupils (which lead to undesirable focal-plane Airy pattern leaks) to azimuthal vortex-phase terms that send light outside the Lyot-plane pupil stop, where they can be blocked. If so, the net mask leakage should be significantly lower in 3-layer masks with unequal topological charges.

$$E_o = \begin{bmatrix} 1 \\ 0 \end{bmatrix}$$

V_1:

$$E_1 = \begin{bmatrix} \eta_1 \\ e^{i2n_1\alpha} \end{bmatrix}$$

V_2:

$$E_2 = \begin{bmatrix} \eta_1\eta_2 + e^{i2(n_1-n_2)\alpha} \\ \eta_1 e^{i2n_2\alpha} + \eta_2 e^{i2n_1\alpha} \end{bmatrix}$$

V_3:

$$E_3 = \begin{bmatrix} \eta_1\eta_2\eta_3 + \eta_3 e^{i2(n_1-n_2)\alpha} + \eta_2 e^{i2(n_1-n_3)\alpha} + \eta_1 e^{i2(n_2-n_3)\alpha} \\ e^{i2(n_1-n_2+n_3)\alpha} + \eta_1\eta_3 e^{i2n_2\alpha} + \eta_2\eta_3 e^{i2n_1\alpha} + \eta_1\eta_2 e^{i2n_3\alpha} \end{bmatrix}$$

= 7 vortex phase terms + 1 small uniform-phase term proportional to the leakage product

If all n's are equal, this becomes

$$E_3 \text{ (equal } n_i) = \begin{bmatrix} \eta_1\eta_2\eta_3 + \eta_3 + \eta_2 + \eta_1 \\ e^{i2(n_1-n_2+n_3)\alpha} + \eta_1\eta_3 e^{i2n_2\alpha} + \eta_2\eta_3 e^{i2n_1\alpha} + \eta_1\eta_2 e^{i2n_3\alpha} \end{bmatrix}$$

~ 4 vortex terms + 3 uniform leakage terms proportional to the first power of leakage

Fig. 16. *Top to bottom:The electric field Jones vector in the circular-polarization basis, and its evolution (downward) through the three layers of a broadband vortex phase mask (shown in blue). The bottom line gives the simplified field that results if* $n_1 = n_2 = n_3$. *Note that the bottom Jones vector includes 4 terms without any phases, which remain inside the pupil, but the equation above it for the case of unequal topological charges contains only one phase-free term. All other 7 terms contain azimuthal vortex phase terms, and so are sent outside the pupil, where they are blocked.*

As a result, three-layer VV masks with unequal charges should leave only a single very dim uniform-pupil leakage term. Moreover, this term, rather than being linearly proportional to any single layer's phase error, is instead proportional to the product of all three small phase errors (one from each layer), and so should be very faint. This in turn should translate to a leakage vs. frequency that can be much broader, with a consequent reduced sensitivity to layer errors, as can be seen in the theoretical predictions of Fig. 17 (Beamco, private communication). With relaxed tolerances, such masks should thus be much easier to manufacture accurately without needing many tries.

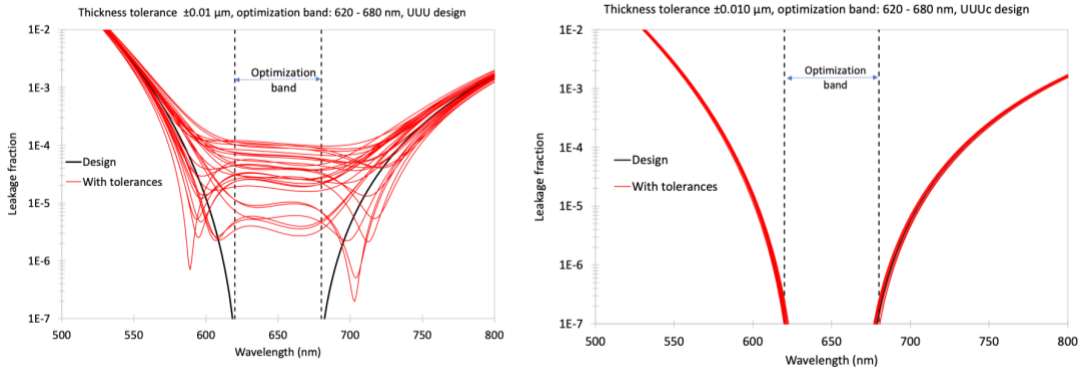

Fig. 17. *Expected mask retardances vs. wavelength for layer tolerances of 1.0% for "classical" VV masks with all layer charges equal (left) and with three different layer charges (right).*

Beamco has manufactured a first vortex mask of this design, with the three different charges as shown in Fig. 18. Note that with unequal charges, the Pancharatnam waveplate broad-banding approach is inoperative, since the relative orientations vary across the device. However, in this case, 6 out of 7 leakage terms have vortex phases, so they should be blocked by the Lyot stop. Thus, leakage elimination in the two cases are quite different: in the Pancharatnam case, spectral polarization broadening is required to reduce leakage, but in the unequal charge case, it may not be, as the Lyot stop should do all the work.

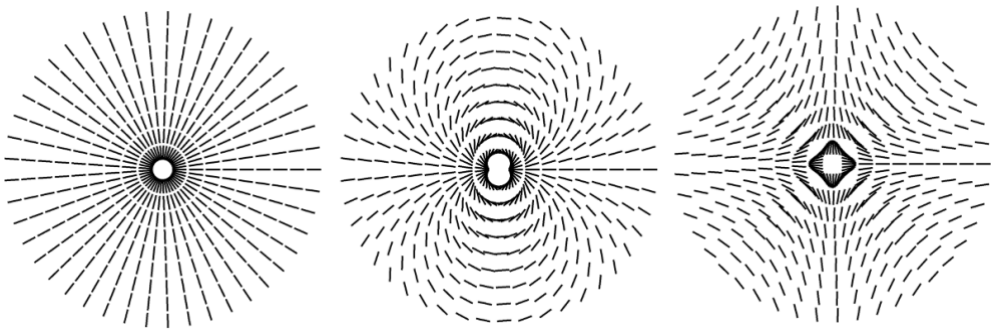

Figure 18. *The three layers in a 3-layer vortex mask with unequal charges 1, 2, and -1. A first mask of this type has been fabricated by Beamco.*

Contrast performance tests of the first mask of this type have been carried out in the DST, but so far have found performance similar to normal VV masks, i.e., within a factor of two of our best classical VV mask. This is not as expected, and we are investigating why the performance was not better. However, the fact that all recently fabricated LCP VV masks of all types yield very similar contrast performances (to within about a factor of 2), including this new type of mask, for which layer thickness errors should be much less important, suggests that it may not actually be the mask fabrication errors of, e.g., layer thickness and layer rotation angle, that are the limiting factor. Indeed, this suggests re-examining other issues, such as the effect of the central defect, and brings added weight to the need to carry out the aforementioned dot/no-dot test, to definitively measure the effect of the central blocker. Delving further into both the theory and into all possible error budget terms in the mask design are thus needed to understand this intriguing result.

The third mask limitation is the presence of small off-axis defects (Fig. 4; center), due likely to small dust particles between the layers or crystallization centers within the layers. These limit broadband wavefront control because the correction of a fixed phase defect in the focal plane using a pupil-plane deformable mirror (DM) requires waves on the DM with different spatial frequencies for each wavelength in the band. These defects have been getting better over the years, and Beamco's new automated coating chamber will help improve mask quality in this regard, both by providing more controllable conditions, and by eliminating human-intervention steps that increase the possibility of contamination.

The planned steps to improved broadband VV mask fabrication and performance thus include the dot/no dot comparison test, in-depth broadband mask modeling and tolerancing to optimize manufacturing techniques, a detailed mask error analysis, new mask designs that are more resilient to manufacturing tolerances, and improved fabrication processes.

4. Testbed Descriptions

Our three milestones will require the DST for ultimate performance, but initial tests of the less mature SV technologies can be carried out in the IACT. Initial mask characterization and vetting will be carried out with our laboratory measurement suite, which includes a polarizing microscope, a Zygo interferometer, An Axoscan Muller Matrix Imaging Polarimeter microscope, and a digital holographic microscope.

4.1. The DST

The DST optical system[4] (Fig. 19) resides in a vacuum chamber that can be evacuated to ~10 milliTorr. For VV work, we modify the standard DST configuration with the addition of two circular polarizers (each of which is composed of a linear polarizer and a quarter-wave retarder). The first circular polarizer will reside inside the light source assembly to generate a single pure circular polarization state, and the second will reside either just after the Lyot stop or the field stop to select the desired output polarization state. All four elements will need to be accurately rotatable, as well as individually removable from the beam, while the DST chamber is under vacuum.

As of March 2019, the DST achieved a mean raw contrast of 4×10^{-10} averaged over angular separations 3-9 λ/D with a bandwidth of $\Delta\lambda/\lambda=0.1$ about $\lambda=550$nm using a Lyot coronagraph in a single polarization (Table 1). With the same setup in monochromatic light, the deepest raw contrast was 2×10^{-10} with the same dark hole region.

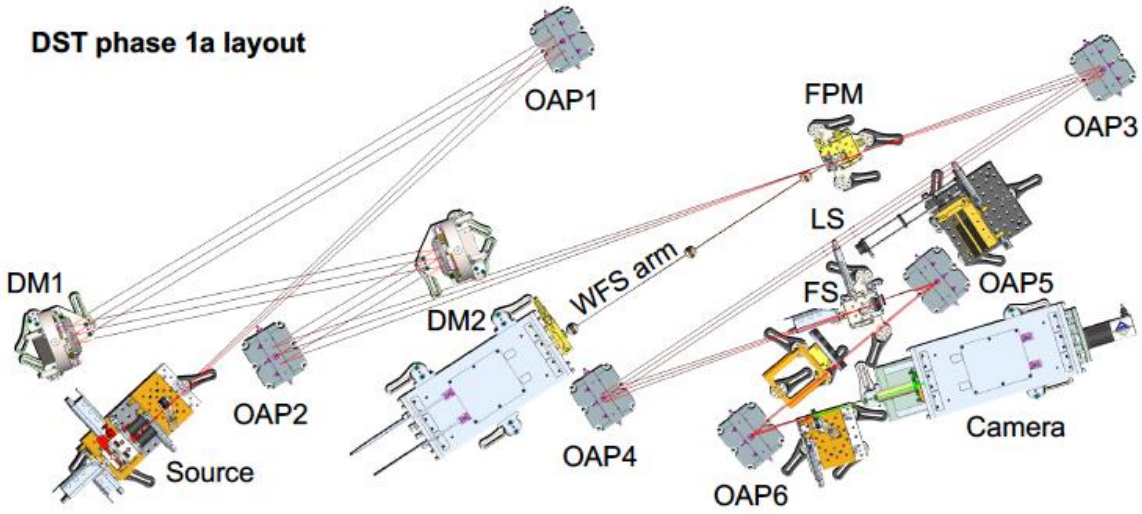

Figure 19. *Optical layout of the DST. OAP = off-axis paraboloidal mirror. DM = deformable mirror. FPM = focal plane mask. LS = Lyot stop. FS = field stop.*

4.2. IACT

This in-air coronagraphic testbed[45] at JPL is similar to the DST, except that it operates in the open air, and has only a single DM. Its layout is shown in Fig. 20. It will be used for initial vetting of SV masks to the 10^{-8} contrast level, after which they will be tested in the DST. The IACT is largely under the control of one of our coIs, Dr. Gareth Ruanne, and so is more readily accessible.

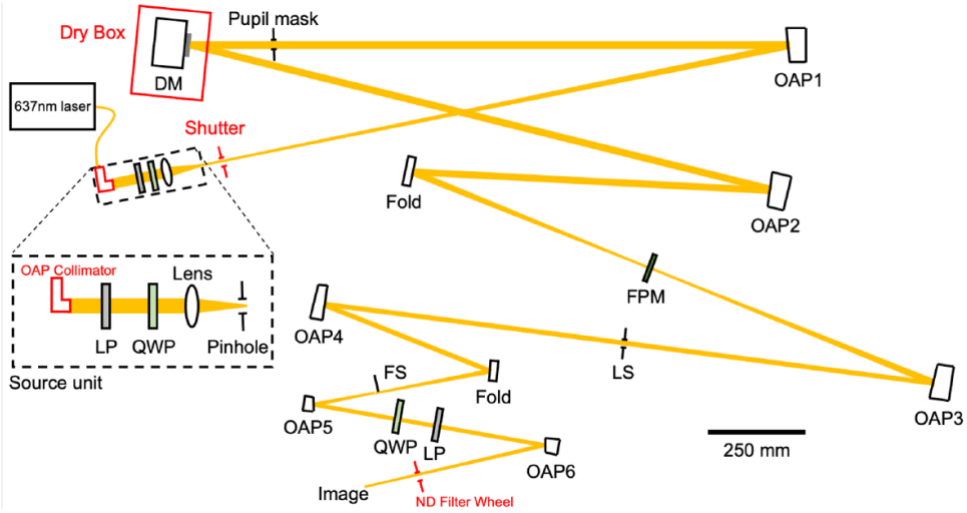

Figure 20 *Layout of the IACT*[45]

4.3. Wavefront Control

Our milestone demonstrations will rely on a wavefront sensing and correction process that has been used in several previous JPL high-contrast demonstrations, including our earlier vortex work. A variant of the "electric field conjugation method" (EFC)[46,47], is used and iterated as necessary. For a given wavelength, and starting with a nominally flat surface figure setting on the DM, one: (a) takes a set of contrast field images with the initial DM setting; (b) takes images for each of four "probe" DM settings (consisting of small deterministic surface figure deviations from the initial DM setting), (c) uses these data to compute the complex electric field in the target dark field region; and then (d) calculates and applies a new DM setting that will reduce the energy over the dark field, thus establishing a new "initial DM setting" in preparation for the next iteration, which is a loop back to step (a). A typical integration time for an individual image is expected to be 10 - 100 seconds, and a complete wavefront sensing and control cycle, including CCD readout overheads, data handling and computations, is expected to take several minutes.

4.4. Differences Between Flight and Laboratory Demonstrations

The DST and IACT coronagraph layouts in the laboratory are similar to coronagraphs being proposed for future flight implementations on HWO, but there are differences.

Light intensity: The spectrum of starlight arriving at a coronagraph would resemble black body radiation, while the source for these milestones will be a broadband supercontinuum source filtered to the desired passband. This source provides a photon flux that is comparable to or somewhat brighter than the target stars to be observed. The goal of these milestones is to demonstrate the contrast that can be achieved with a vortex coronagraph, independent of the source intensity. A bright source is a convenience that does not compromise the integrity of the demonstration, as it affects only the integration times.

Light spatial uniformity: Unlike the light incident on a telescope from a target star, the light intensity in the testbeds is not uniform across the pupil. Typically, the light intensity drops center-to-edge by a few percent, due to the diffraction pattern from the small source pinhole. This small non-uniformity is expected to have a negligible effect on the final contrast if it is accounted for in the wavefront control algorithm, and a small but below-requirement loss of contrast if it is ignored in the control algorithm.

Number of polarization states: The laboratory setup will probe the need to separate polarization states to reach high contrast. Our input circular polarizer will be located upstream of the pinhole, which is not where it would be in any flight system, where it would need to be located in a more spatially extended beam. Our goal is therefore to show that a dark hole of the requisite depth can be generated in this more ideal single-polarization situation. For the SV case, we hope to be able to dispense with the circular polarizers.

Number of deformable mirrors: Both in the laboratory and in space, highest contrasts call for two DMs in the optical system, in order to allow for the control of both phase and amplitude errors in the complex wavefront and to provide better broadband control through the Talbot effect, wherein phase deviations applied with a DM not located in a pupil plane are converted to pupil-plane intensity variations upon propagation. The DST makes use of a pair of DMs, as is planned for future high-contrast space missions, and is thus essential to meeting our contrast requirements.

Spacecraft dynamics: A control system is required in flight to stabilize the light path against motions of the spacecraft. The dominant effects of spacecraft dynamics are jitter of the stellar image on the coronagraphic focal plane mask and beam walk in the optics upstream of the mask. As a specific example, the ACCESS analysis[48] showed that for 4th-order coronagraphs (including Lyot, vortex, and pupil mapping coronagraphs) with an inner working angle of $3\lambda/D$, rms pointing errors need to be $< \pm 0.03\ \lambda/D$ to limit the contrast degradation to $< 2\times10^{-10}$. Concept models have shown that this required pointing stability can be achieved in space with current high Technology Readiness Level (TRL) systems. In the DST, this would correspond to an ability to center the vortex mask on the "star" within about 2.5 μm, or about 0.2 pixel when projected to the CCD focal plane.

The milestone demonstrations require passive stability of the testbed, which is thus untraceable to spacecraft dynamics. In practice, the DST may exhibit alignment drifts that

are larger than expected in the space environment. If so, we will rely on favorable periods of thermal and mechanical stability of the DST.

5. Data Measurement and Analysis

A contrast measurement is a measurement of the intensity of the residual light (speckles, background, etc.) within the dark field, relative to the peak intensity of an image of the source. There will of course be a distribution of intensities across the dark hole, from which the average contrast and its statistical confidence level will be calculated. The milestone objective is to demonstrate with high confidence ($\geq$ 90%) that the true contrast in the dark field, as estimated from our measurements in the presence of noise, is equal to or better than the required threshold contrast, e.g., $c_0 = 5.0 \times 10^{-10}$.

Because of laboratory instabilities and the ongoing wavefront control algorithm, the contrast at any point in the dark field is time dependent, and so multiple successive exposures of the dark hole will be taken. For each image (where "each image" can itself be more than one sequential image if temporal averaging is deemed important to build up signal to noise), we calculate a spatial average of the measured contrast level over the entire dark hole. This yields a series of n (with $n \geq 4$) individual dark hole images, each with its own spatially-averaged dark hole contrast, c_i. We next take an average over the series of n dark hole images, leading to a sample-averaged contrast and variance, both defined below. To avoid confusion, we refer to spatial averages over an image region as "averages", and averages of quantities over a number (sample) of images as "means". Finally, we note that the entire experimental run is then to be repeated from scratch at least 3 times, to show repeatability. No averaging is done over the independent runs, so that the milestone is achieved independently m times.

As mentioned, the measured contrast is time dependent, being subject to laboratory conditions such as the quality of the optical components, their alignment, drifts in their alignment over time, and the effectiveness of each wavefront sensing and control cycle. With each iteration, the wavefront sensing and control procedure attempts to improve the contrast, thus compensating for any drift or alignment changes that may have occurred since the previous iteration. Further variations may be expected due to experimental noise and any limitations in the algorithm. The images built up from a sequence of such iterations will provide a distribution of contrast values, which will be regarded as Gaussian about a mean contrast for the data set. We therefore consider the mean contrast value as representative of the true contrast value for a given data set.

The contrast measurements of the iterations within a single run will fluctuate due to both random wavefront control errors and random measurement errors. The statistical confidence level will thus require an estimation of the variance. Given that our speckle fields contain a mix of static and quasi-static speckles (the residual light field remaining after the completion of a wavefront sensing and control cycle, together with the effects of alignment drift following the control cycle), as well as other sources of measurement noise including photon detection statistics and CCD read noise, an analytical development of speckle statistics is impractical. We will thus compute the confidence levels under the

assumption of Gaussian statistics. (The full set of measurement will also be stored, to enable computation of the confidence levels for other statistics.)

The following paragraphs define the terms involved in the measurement process, spell out the measurement steps, and specify the data products.

5.1. Definitions

5.1.1. "Raw" Image and "Calibrated" Image. Standard techniques for the acquisition of CCD images are used. A "raw" image is the pixel-by-pixel image obtained by reading the charge from each pixel of the CCD, and amplifying and sending it to an analog-to-digital converter. A "calibrated" image is a raw image that has had background bias subtracted and the detector responsivity normalized by dividing by a flat-field image. (Saturated images are avoided in order to avoid the confusion of CCD blooming and other potential CCD nonlinearities.) A calibrated image can also include the step of low-order aberration contribution subtraction based on wavefront information provided by a low-order wavefront sensor, if one is available).

5.1.2. "Scratch" is a DM setting in which actuators are set to a predetermined surface figure that is approximately flat (typically, about 20 volts on each actuator).

5.1.3. The "algorithm" is the computer code that takes as input the measured speckle field images, and produces as output a voltage value to be applied to each element of the DM, with the goal of reducing the intensity of speckles.

5.1.4. The "star" is a small pinhole illuminated with laser or broadband light relayed via optical fiber from a source outside the chamber's vacuum wall (e.g., a laser or a filtered super-continuum white light source). The "small" pinhole is to be unresolved by the optical system; e.g., a 5-μm diameter pinhole would be "small" and unresolved by the 80-μm FWHM Airy disk in an f/100 beam at 600 nm wavelength. This "star" is the only source of light in the optical path of the coronagraph. It is a stand-in for the star image that would have been formed by a telescope system.

5.1.5. The "contrast field" is a dimensionless map representing, for each detector pixel, the ratio of its value to the value of the peak pixel of the PSF that would be measured in the same testbed conditions (light source, exposure time, Lyot stop, etc.) if the vortex mask were removed. The calibration of the contrast field is discussed in Section 5.3.

5.1.6. The "average contrast", c_i, is a dimensionless quantity that is, for a given image, the spatial average value of the contrast field over the defined dark hole. Explicitly, an image's average contrast is the sum of the contrast values for all pixels in the dark field, divided by the total number of pixels in the dark field, with no weighting applied.

5.1.7. The "mean contrast", $\hat{c}$, of a given sequence of $n \geq 4$ images is the mean of the individual average contrast values occurring in that sequence:

$$\hat{c} = \frac{1}{n}\sum c_i.$$

5.1.8. "Milestone metric": ĉ is the milestone metric.

5.1.9. "Standard Deviation": The standard deviation σ_{meas} for an individual measurement of the average contrast value c_i of a sequence of contrast images given as usual by:

$$\sigma_{meas} = \sqrt{\sum_{i=1}^{n} \frac{(c_i - \hat{c})^2}{n-1}}$$

The uncertainty in the mean contrast ĉ is then given by

$$\sigma_{mean} = \frac{\sigma_{meas}}{\sqrt{n}}.$$

There is also a contribution to the uncertainty from the independently-determined photometry error, σ_{phot}. The net standard deviation is thus

$$\sigma = \sqrt{\sigma_{mean}^2 + \sigma_{phot}^2}$$

5.1.10. "Statistical Confidence". For contrast values that have a Gaussian distribution about the mean contrast, the statistical confidence that the mean contrast ĉ is less than some value c_0 is given by

$$conf(z < t) = \frac{1}{\sqrt{2\pi}} \int_{-\infty}^{t} e^{-z^2/2}\, dz = \frac{1}{2} + \frac{1}{\sqrt{2\pi}} \int_{0}^{t} e^{-z^2/2}\, dz$$

where $t = (c_0 - \hat{c})/\sigma$. Thus, as $\hat{c} = c_0 - t\sigma$, meeting a milestone contrast target c_0 with the desired confidence level requires the final measured mean contrast for a given run, ĉ, to be lower than the target contrast c_0 by t standard deviations. The Gaussian integral is widely tabulated, and *conf* = 0.9 implies t = 1.28. Thus, for 90% confidence, $\hat{c} = c_0 - 1.28\sigma$, i.e., the measured ĉ is smaller than the target c_0 by 1.28σ.

5.2. Measurement of the Star Brightness

5.2.1. The vortex mask is displaced laterally relative to the center of the beam by approximately 10 λ/D or so, so as to transmit maximum stellar flux.

5.2.2. To create the photometric reference, a representative sample of short-exposure (e.g. a few milliseconds) images of the star is taken, with all coronagraph elements other than focal-plane vortex mask in place.

5.2.3. The images are averaged to produce a single star image. The "short-exposure peak value" of the star's intensity is estimated. Since the star image is well-sampled in the CCD focal plane (the Airy disk can be sampled by ~20 pixels within a radius equal to the full width half maximum), the star intensity can be estimated using either the value of the maximum-brightness pixel or an interpolated value representative of the apparent peak.

5.2.4. The "peak count rate" (counts/sec) is measured for exposure times of microseconds to tens of seconds.

5.3. Measurement of the Coronagraph Dark Hole Contrast Field

5.3.1. The vortex mask is centered on the star image.

5.3.2. An image with a typical exposure time of several seconds is taken of the coronagraph field (the suppressed star and surrounding speckle field). The target dark hole is a D-shaped field extending from 3 to 10λ/D, bounded by a straight line passing 3λ/D from the star at its closest point, and by a circle of radius 10 λ/D centered on the star (shown in Fig. 1).

5.3.3. The image is normalized to the "star brightness" as defined in 5.2, using the fixed ratio between peak star brightness and the integrated light in a region of the speckle field outside the central DM-controlled area. I.e., dark-hole/star = dark-hole/speckle * speckle/star. For this purpose, any well-defined region of the outer speckle field can be used; the red region in Figure 21 (taken from ref 49) is only illustrative.

(In slightly more detail, to avoid saturation issues with the full-flux image case, there are usually three ratios involved: dark hole pixel/distant speckle field (both obtained with the vortex in); distant speckle field/inner point spread function [out to several Airy rings (about 200 pixels); both obtained with vortex out]; and inner point spread function/central point spread function pixel [both with vortex out]). In our previous TDEM work, we found the distant speckle field to be unchanged by the insertion or removal [by lateral translation] of the vortex, thus providing a robust calibration ladder. Other calibration ladders may also be possible.

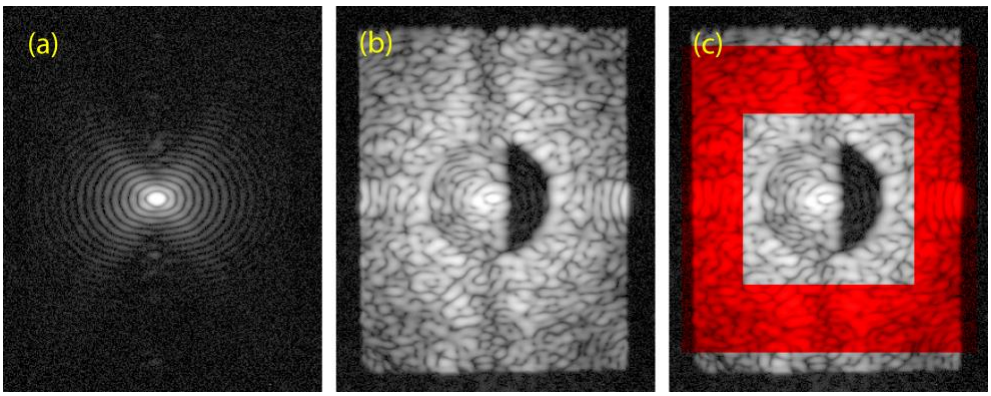

Figure 21. *Reference field for contrast photometry. Shown here are (a) the "star" reference image, (b) the high-contrast coronagraph field; and (c) the same with a region of the reference speckle field in the "uncontrolled" area beyond the DM's Nyquist limit superimposed in red. (Any subset of the red region can be used). Images are displayed with a logarithmic contrast stretch.*

5.4. Milestone Demonstration Procedure

5.4.1. The DM is set to scratch. An initial coronagraph contrast field image is obtained as described in Sec. 5.3.

5.4.2. Wavefront sensing and control is performed to find settings of the DM actuators that give the required high-contrast in the target dark field. This iterative procedure may take from one to several hours, starting from scratch, if no prior information is available. However it can take more or less time depending on the stability of the optical system.

5.4.3. A number of contrast field images are taken, following steps 5.4.1 – 5.4.2. A sufficient number (≥ 4) of images are taken to provide statistical confidence that the milestone contrast levels have been achieved, as described in Section 5.1.

5.4.4. Laboratory data are archived for future reference, including all raw images of the reference star and contrast field images.

5.5. Milestone Data Package

The milestone certification data package will contain the following:

5.5.1. A narrative report that includes a discussion of how each element of the milestone was met, with a narrative summary of the overall milestone achievement and its repeatability.

5.5.2. A description of the optical elements, including the vortex masks, and their significant characteristics.

5.5.3. A tabulation of the significant operating parameters of the apparatus.

5.5.4. A representative contrast field image from the set of images used in the statistical analysis of the milestone, with appropriate numerical contrast values indicated, with coordinate scales indicated in units of Airy distance (λ/D).

5.5.5. A description of the data reduction algorithms, in sufficient detail to guide an independent analysis of the delivered data.

5.5.6. Average and mean contrast values and standard deviations for the data used to satisfy the milestone requirements.

5.5.7. For each image reported as part of the milestone demonstration, the average contrast within the area spanning 3-4 λ/D.

6. Success Criteria

The following are the required elements of the milestone demonstration. Each element includes a brief rationale.

6.1. Illumination is single or dual polarization at a wavelength in the range of 300 nm $< \lambda <$ 1000 nm, for 10% or 20% bandwidth, depending on the specific milestone.

Rationale: *This milestone is an initial demonstration of the feasibility of the approach at a wavelength in the science band of HWO.*

6.2. The contrast specified in each milestone in Section 3 shall be achieved in a 3 to 10 λ/D dark zone, using the basic geometry of Fig. 1.

Rationale: *This provides evidence that the high contrast field is sufficiently dark to be useful for searching planets, yet within proven testbed performance capabilities*.

6.3. Criterion 6.2 shall be met with a confidence of 90% or better. Sufficient data must be taken to justify this statistical confidence.

Rationale: *Assuming the contrasts have a Gaussian distribution about the mean, this demonstrates a statistical confidence of 90% that the contrast goal has been met.*

6.4. Elements 6.1 – 6.3 must be satisfied on 3 separate occasions with a reset of the wavefront control system software (DM set to scratch) between each demonstration.

Rationale: *This provides evidence of the repeatability of the contrast demonstration*.

The wavefront control system software reset between experimental runs ensures that the different data sets can be considered as independent and do not represent an unusually good configuration that cannot be readily reproduced. For each demonstration, the DM will begin from a "scratch" setting. There is no time requirement for the demonstrations, other than the time required to meet the statistics stipulated in the success criteria. There is no required interval between demonstrations; subsequent demonstrations can begin as soon as prior demonstrations have ended. There is also no requirement to turn off power, open the vacuum tank, or delete data relevant for the calibration of the DM influence function.

7. Work Plan and Schedule

Our work plan consists of three almost-annual cycles consisting of a five-phase sequence. Each cycle begins with device modeling, followed by negotiation with vendors, the design and delivery of the next generation of vortex phase mask, the vetting of these masks in the IACT and in our various other test equipment, and then finally, high-contrast performance testing in the DST. An annual schedule can thus be defined based on the high-contrast performance goals for each new generation of mask. However, as the three different mask technologies have different maturity levels, their performance expectations are staggered relative to each other. Ultimately, dark-hole contrast demonstrations at DST best contrast levels are targeted for each type of mask, with contrasts decreasing and bandwidths increasing as a function of time.

Our annual performance targets, which feed into our three milestones, are as follows. Note that our three annual targets for the LCP masks are exactly the same as our three official milestones, as this is currently the most advanced technology. Given our recent modeling results, we expect that the structured glass scalar vortex masks will likely not be far behind in time, after an initial catch-up phase. However, we retain a more conservative approach to the metasurface masks, as there is still much to learn about that approach.

1. Liquid crystal polymer masks:
   year 1: 1.6×10^{-9} for 20% BW
   year 2: DST best level for 10% BW
   year 3: DST best level for 20% BW

2. Structured glass scalar vortex masks:
   year 1: 10^{-9} for 10% BW
   year 2: 10^{-9} for 20% BW
   year 3: DST best level for 20% BW

3. Metasurface masks
   year 1: 10^{-8} for 10% BW
   year 2: 10^{-9} for 10% BW
   year 3: DST best level for 10% BW

In practice, the "annual" cycle will be slightly longer than a year. In particular, the needed modeling for the next mask will be carried out before each performance year begins, especially as we already have models in hand. Thus in practice, the modeling for the next yearly set of masks will be carried out while the previous year's DST run is proceeding (or before the official project start by already funded postdocs), thus allowing a full 6 months to negotiate with vendors and to manufacture the next generation of masks. It will thus be approximately 14 months from "next model start" to "end of annual tests", meaning two months of overlap between the approximately "annual" cycles.

In more detail, within each cycle, there will be two months for modeling, 1-2 months for discussions with vendors, 4-5 months for manufacture of next generation masks (as well as for the preparation of any ancillary optics), 2 months for mask vetting with our microscopes and the IACT, and finally, a 4 month long DST test run, during which the next set of modeling will begin. Based on past experience, the DST runs may not be so

rigidly delineated, as we are happy to share our runs with other TDEM projects to maximize overall efficiency.

The annual performance goals are directly tied to mask improvement steps. For the scalar masks, there are three necessary steps. First, we will develop and test the performance of a single-glass dimpled SV mask, then we will show that this same structure can be manufactured in TiO_2, so that we have both glasses that we need for a broadband SV mask, and finally we will combine both types of glasses. We will also investigate the manufacture of the needed structures in the other identified materials, but we will start with the easiest choice of fused silica and TiO_2. Of course, there will also be ancillary steps, such as the mount for holding the two component masks together, as needed. For the LCP masks, the steps will be to investigate the non-equal charge masks first to see if the bandwidth can be increased and the tolerances eased, then the mask quality addressed to go deeper, and then both will be combined. In the metasurface case, we will need a year to establish metasurface manufacturing processes, and then a year to develop broadband techniques, and a third year to optimize processes.

Regarding the division of effort between the mask types, two NASA Postdoctoral Fellows (NPPs) at JPL are participating in this project, one an expert in metasurfaces (Lorenzo Koenig), and one an expert in glass vortex structures (Niyati Desai), while the PI is an expert in LCP masks. Therefore each of the three mask types to be developed has an in-house expert to independently guide the development of that type of mask. The work on the three mask types is thus decoupled (except for oversight by the PI) and can proceed in parallel. Moreover, while the Exoplanet program's DST team will carry out the high contrast tests in the DST, the two NPPs involved will lead the IACT tests, as they are already up to speed on that more accessible testbed. The IACT is much more readily accessible, and so preliminary IACT tests can be fit in as needed, but some coordination will of course be needed to have the IACT available prior to the DST runs. The current DST schedule shows this project as having first access to the DST in August and September of 2026, but the relevant DST schedule is currently undefined beyond that. We also note that the DST schedule is not immutable, and has been shifted in the past to optimize utilization, and we expect similar occurences in the future.

Finally, we note that the JPL facility team will be responsible for all DST assembly and alignment steps, for all control and dark-hole generation software, and for any upgrades to the DST facility. As a result, the facility team may need additional DST time outside of our official TDEM test runs for such work. We will, however, be happy to work with the DST team to mesh our respective tasks in order to optimize the facility schedule.

8. References

1 2020 Decadal Survey for Astronomy and Astrophysics, "Pathways to Discovery in Astronomy and Astrophysics for the 2020s", The National Academies Press, Washington, DC (2021)

2 https://science.nasa.gov/astrophysics/programs/habitable-worlds-observatory/

3 B. Mennesson et al. “Current laboratory performance of starlight suppression systems, and potential pathways to desired Habitable Worlds Observatory exoplanet science capabilities,” J. Astron. Tel. Instr. Sys., 10, 035004 (2024)

4 Ruane, G. et al., “Decadal Survey Testbed Commissioning Roadmap: Demonstrating Technology for Imaging New Worlds,” (2019) https://exoplanets.nasa.gov/internal_resources/1170/

5 K. Stapelfeldt et al. “Exo-C: a probe-scale space mission to directly image and spectroscopically characterize exoplanetary systems using an internal coronagraph,” Proc. SPIE 9143, 91432K (2014)

6 Gaudi, B., Seager, S., Mennesson, B., Kiessling, A., Warfield, K., Cahoy, K., Clarke, J., Domagal-Goldman, S., Feinberg, L., Guyon, O. et al.: “The Habitable Exoplanet Observatory (HabEx) mission concept study final report”, arXiv preprint, arXiv:2001.06683 (2020)

7 Fischer, D., Peterson, B., Bean, J., Calzetti, D., Dawson, R., Dressing, C., Feinberg, L., France, K., Guyon, O., Harris, et al., “The LUVOIR mission concept study final report”, arXiv preprint, arXiv:1912.06219 (2019).

8 Foo, G., Palacios, D. M. and Swartzlander, Jr., G. A., “Optical Vortex Coronagraph,” Opt. Lett. 30, 3308 (2005)

9 Swartzlander, G., “The optical vortex coronagraph, ” J. Opt. A., 11, 1464 (2009)

10 Mawet, D., Riaud, P., Absil, O. and Surdej, J., “Annular Groove Phase Mask Coronagraph” ApJ, 633, 1191 (2005)

11 Mawet, D. et al., “Optical Vectorial Vortex Coronagraphs using Liquid Crystal Polymers: Theory, Manufacturing and Laboratory Demonstration,” Opt. Exp., 17, 1902 (2009)

12 Ruane et al., “Performance and sensitivity of vortex coronagraphs on segmented space telescopes” Proc. SPIE 10400, 104000J (2017)

13 Mawet, D. et al., “Taking the vector vortex coronagraph to the next level for ground- and space-based exoplanet imaging instruments: review of technology developments in the USA, Japan, and Europe,” Proc. SPIE 8151, 815108-1 (2011)

14 Serabyn, E., Mawet, D. and Burruss, R., “An image of an exoplanet separated by two diffraction beamwidths from a star”, Nature, 464, 1018-1020 (2010)

15 Mawet, D., Absil, O., Delacroix, C., Girard, J., Milli, J., O’Neal, J., Baudoz, P., Boccaletti, A., Bourget, P., Christiaens, V. et al.: “L’-band AGPM vector vortex coronagraph’s first light on VLT/NACO. Discovery of a late-type companion at two beamwidths from an F0V star”, Astronomy & Astrophysics 552, L13 (2013)

16 Defrère, D., Absil, O., Hinz, P., Kuhn, J., Mawet, D., Mennesson, B., Skemer, A., Wallace, K., Bailey, V., Downey, E. et al.: “L’-band AGPM vector vortex coronagraph’s first light on LBTI/LMIRCam”, Proc. SPIE 9148, 91483X (2014)

17 Kühn J. et al., “An H-band vector vortex coronagraph for the Subaru coronagraphic extreme adaptive optics system”, Publ. Astron. Soc. Pac. 130(985), 035001 (2018)

18 Serabyn, E. et al., “The WM Keck observatory infrared vortex coronagraph and a first image of HIP 79124 B”, Astron. J. 153(1), 43 (2017)

19 Serabyn, E., et al., “Vector vortex coronagraphy for exoplanet detection with spatially variant diffractive waveplates,” JOSA B 36(5), D13-D19 (2019)

20 Swartzlander, G.A., Ford, E.L., Abdul-Malik, R.S., Close, L.M., Peters, M.A., Palacios, D.M. and Wilson, D.W., “Astronomical demonstration of an optical vortex coronagraph”, Optics Express 16(14), 10200-10207 (2008)

21 Desai, N., Ruane, G., Llop-Sayson, J., Betrou-Cantou, A., Potier, A., Riggs, A., Serabyn, E. and Mawet, D.: “Laboratory demonstration of the wrapped staircase scalar vortex coronagraph”, J. Astron. Tel. Instr. Sys. 9(2), 025001 (2023)

22 R. Galicher et al., “A family of phase masks for broadband coronagraphy example of the wrapped vortex phase mask theory and laboratory demonstration,” Astron. Astrophys. 635, A11 (2020).

23 S. Palatnik et al., “Optimizing metasurfaces to achieve deeper direct imaging contrasts: analyses of current performance and lessons learned from fabrication,” Proc. SPIE 13100, 1310063 (2024)

24 L. König, N. Desai, S. Palatnick, O. Absil, D. Mawet, M. Millar-Blanchaer, E. Serabyn, “Microstructured vortex and azimuthal cosine phase mask design for high-contrast imaging,” J. Astron. Tel. Instr. Sys. 11(2), 025002-1 (2025)

25 Llop-Sayson, J., Ruane, G., Serabyn, E., Mejia Prada, C., Walter, A., Allan, G. “Vector Vortex Coronagraph Experiments in Vacuum Towards 10^{-10} Contrast,” Proc. SPIE 13092, 130921Y (2024)

26 Ruane, G., Riggs, A., Serabyn, E., Baxter, W., Mejia Prada, C., Mawet, D., Noyes, M., Poon, P. and Tabiryan, N.: “Broadband vector vortex coronagraph testing at NASA’s high contrast imaging testbed facility”, Proc. SPIE 12180, 1218024 (2022)

27 N. Desai, D. Mawet, E. Serabyn, G. Ruane, A. Bertrou-Cantou, J. Llop-Sayson, A. J. Eldorado Riggs, “Benefits of adding radial phase dimples on scalar coronagraph phase masks,” J. Astron. Tel. Instr. Sys. 10(1), 015001 (2024)

28 G. A. Swartzlander, “Achromatic optical vortex lens,” Opt. Lett. 31, 2042–2044 (2006)

29 Roddier, F. and Roddier, C.: “Stellar coronagraph with phase mask”, Publications of the Astronomical Society of the Pacific 109(737), 815 (1997)

30 Yu, N. and Capasso, F.: “Flat optics with designer metasurfaces”, Nature Materials 13(2), 139-150 (2014)

31 Kruk, S., Ferreira, F., Mac Suibhne, N., Tsekrekos, C., Kravchenko, I., Ellis, A., Neshev, D., Turitsyn, S. and Kivshar, Y.: “Transparent dielectric metasurfaces for spatial mode multiplexing”, Laser & Photonics Reviews 12(8), 1800031 (2018)

32 Khorasaninejad, M., Chen, W., Devlin, R., Oh, J., Zhu, A. and Capasso, F.: “Metalenses at visible wavelengths: Diffraction-limited focusing and subwavelength resolution imaging”, Science 352(6290), 1190-1194 (2016)

33 Devlin, R., Ambrosio, A., Wintz, D., Oscurato, S., Zhu, A., Khorasaninejad, M., Oh, J., Maddalena, P. and Capasso, F.: “Spin-to-orbital angular momentum conversion in dielectric metasurfaces”, Optics Express 25(1), 377-393 (2017)

34 Chong, K., Staude, I., James, A., Dominguez, J., Liu, S., Campione, S., Subramania, G., Luk, T., Decker, M., Neshev, D. et al.: "Polarization-Independent Silicon Metadevices for Efficient Optical Wavefront Control", Nano Letters 15(8), 5369-5374 (2015)

35 Shalaev, M., Sun, J., Tsukernik, A., Pandey, A., Nikolskiy, K. and Litchinitser, N.: "High-Efficiency All-Dielectric Metasurfaces for Ultracompact Beam Manipulation in Transmission Mode", Nano Letters 15(9), 6261-6266 (2015)

36 Heiden, J. and Jang, M.: "Design framework for polarization-insensitive multifunctional achromatic metalenses", Nanophotonics 11(3), 583-591 (2022)

37 Sun, T., Hu, J., Ma, S., Xu, F. and Wang, C.: "Polarization-insensitive achromatic metalens based on computational wavefront coding", Optics Express 29(20), 31902-31914 (2021)

38 Li, X. and Fan, Z.: "Controlling Dispersion Characteristic of Focused Vortex Beam Generation", Photonics 9(3), 179 (2022)

39 Shrestha, S. et al., Light: Science & Applications 7(1), 85 (2018)

40 Riggs, A., Ruane, G., Sidick, E., Coker, C., Kern, B. and Shaklan, S.: "Fast linearized coronagraph optimizer (FALCO) I: a software toolbox for rapid coronagraphic design and wavefront correction", Proc. SPIE 10698, 878-888 (2018)

41 Pancharatnam, S., "Achromatic combination of birefringent waveplates," Proc. Indian Acad. Sci. A 41, 137 (1955)

42 Komanduri, R. K. et al., "Multi-twist retarders for broadband polarization transformation," Proc. SPIE 8279, 82790E (2012)

43 Roberts, D. et al., "Overcoming the tradeoff between efficiency and bandwidth for vector vortex waveplates," Proc. 2019 IEEE Aerospace Conf. (2019) 10.1109/AERO.2019.8741585

44 Roberts, D.E. et al. "Opportunities for next generation vector vortex waveplates," Proc. 2023 IEEE Aerospace Conf (2023) 10.1109/AERO55745.2023.10115753,

45 Baxter, W. et al., Proc. SPIE 11832, 118231S (2021)

46 Give'on, A. et al., "Broadband wavefront correction algorithm for high-contrast imaging systems," Proc. SPIE 6691, 66910A (2007)

47 Give'on, A., "A unified formalism for high contrast imaging correction algorithms," Proc. SPIE 7440, 74400D (2009)

48 Trauger, J. et al., "ACCESS – A Concept Study for the Direct Imaging and Spectroscopy of Exoplanetary Systems," in "Pathways towards Habitable Planets," ASP Conf. Series 430, 375 (2010)

49 Trauger, J. et al., "TPF-C Milestone #1 Report," JPL Document D-35484 (2006)